ADVANCED OPTICAL MATERIALS
www.advopticalmat.de

Correlative Super-Resolution Imaging of Cellular Nanopores Facilitated by Transparent Polymer Waveguide Chips

*Surjendu Bikash Dutta, Jasmin Celine Schürstedt-Seher, Anders Kokkvoll Engdahl, Wolfgang Hübner, Stefan Belle, Karolina Szafranska, Peter McCourt, Ralf Hellmann, Mark Schüttpelz, and Thomas Huser**

Super-resolution optical microscopy (SRM) permits the visualization of subcellular structures of biological samples beyond the diffraction limit of light. To evaluate and utilize the specific strengths of each SRM technique a combined approach in the form of correlative super-resolution imaging is essential. Here, the correlative SRM imaging of the ultrastructure of rat liver sinusoidal endothelial cells (LSECs) across a large field of view (FOV) with 3D structured illumination microscopy (3D-SIM) and single-molecule localization microscopy (SMLM), facilitated by a transparent polymer photonic waveguide chip, is presented. This waveguide is not only used for chip-based total internal reflection fluorescence (TIRF) excitation across a large FOV, but also enables the excitation and collection of single-molecule fluorescence via the inverted microscope configuration. Furthermore, the structural design of the waveguides allows to identify and correlate sample positions across multiple microscopes. This correlative SIM and multi-modality SMLM imaging provides a high throughput (FOV of ≈180 µm × 120 µm) method to analyze the structural morphology of LSECs with high spatial resolution (≈50 nm). Furthermore, waveguide chip-based TIRF excitation also yields a significant reduction of background signals.

1. Introduction

Super-resolution fluorescence microscopy (SRM), commonly known as optical nanoscopy, has shown immense potential to visualize the subcellular structure of biological samples beyond the diffraction limit of light.[1–5] Various SRM techniques, such as structured illumination microscopy (SIM),[6,7] stimulated emission depletion microscopy (STED),[8,9] single-molecule localization microscopy (SMLM),[10–12] and temporal and spatial signal fluctuation-based techniques (SOFI, ESI, (e)SRRF)[13–15] have emerged over the last few years. Each of these techniques has its own advantages and disadvantages and they demonstrate their ability for optical super-resolution depending on specific imaging requirements.[2,5,16,17] The practical implementation of each nanoscopy technique is, however, still limited by their applications due to multiple reasons, such as low throughput, bulky setups, high cost, and complex systems, among others. For example, the ability of SIM to provide video rate imaging speed[18–21] makes it one of the most popular methods among existing optical nanoscopy techniques, specifically for live cell applications, but the resolution improvement is typically limited to a factor of two.[6] SMLM approaches, such as direct stochastic optical reconstruction microscopy (dSTORM),[22] on the other hand, provide high spatial resolution on the order of 10–20 nm, but require rather long overall signal accumulation times because several thousands of frames have to be acquired in order to obtain a reconstructed image with super-resolution.[10,11,22] Therefore, a combined approach that utilizes the specific strengths of each technique is most promising.

In recent years, photonic waveguide chips have been introduced as a versatile platform to perform multimodal optical nanoscopy of biological samples with high throughput and high spatial resolution.[23–27] Waveguide-chip based total internal reflection fluorescence (TIRF) microscopy provides several advantages over the common objective-type TIRF microscopy. In objective-type TIRF microscopy the excitation and emission paths are shared in epi-illumination and detection mode, which restricts this modality to high numerical aperture (NA) lenses.

S. B. Dutta, J. C. Schürstedt-Seher, A. K. Engdahl, W. Hübner, M. Schüttpelz, T. Huser
Biomolecular Photonics
Faculty of Physics
Bielefeld University
Universitätsstraße 25, 33615 Bielefeld, Germany
E-mail: thomas.huser@physik.uni-bielefeld.de
S. Belle, R. Hellmann
Applied Laser and Photonics Group
Aschaffenburg University of Applied Sciences
Würzburger Str. 45, 63743 Aschaffenburg, Germany
K. Szafranska, P. McCourt
Department of Medical Biology
UiT – The Arctic University of Norway
Hansine Hansens veg 18, Tromsø 9019, Norway

The ORCID identification number(s) for the author(s) of this article can be found under https://doi.org/10.1002/adom.202402783

DOI: 10.1002/adom.202402783

This also limits the field of view (FOV) that can be obtained. In waveguide-chip based nanoscopy, an evanescent field is generated on top of the (often high NA) waveguide surface due to total internal reflection within the planar waveguide structure and this field is then used for TIRF excitation. In addition, the photonic chip conveniently also serves as a sample holder to move and register the sample with high reproducibility between different imaging setups. Thus far, most chip-based microscopy has been performed on high refractive index waveguides fabricated on top of opaque substrates, typically silicon wafers, where the sample sits on top of the waveguide. These chips can therefore only be used with an upright microscope because the opaque substrate prevents the light being collected from below the substrate. Some recent studies have, however, already demonstrated concepts for the use of transparent waveguide chips for TIRF microscopy and nanoscopy.[28–30] Here, the transparent photonic chips provide a fairly universal imaging platform, where fluorescence can also be collected through the substrate via the inverted microscope configuration. This allows the use of high-resolution oil immersion objective lenses which are usually aberration-corrected for a 170 µm thick cover glass.[28,29] Opaque waveguide chips, on the other hand, limit imaging to upright configurations and typically employ lower NA air objective lenses.[23–25] Additionally, sample handling is more complicated with opaque chips because access to the sample and imaging can only be performed from the same direction. This creates challenges, especially for biological samples such as cells or tissues where transmission microscopy allows for the easy assessment of the sample.

Few attempts of combining different microscopy methods have been introduced so far, such as multi-modal super-resolution optical microscopy and correlative light and electron microscopy (CLEM).[31–37] For example, Rossberger et al. combined SIM and single molecule localization microscopy into a single optical platform and demonstrated the advantage of this by imaging identical regions of H3K293 cells.[32] Also, Hamel et al. used 3D-SIM to obtain multi-color SIM data and compared them with the higher resolution obtained by single-molecule localization microscopy.[33] Similarly, Mönkemöller et al., demonstrated the complementary use of 3D-SIM and dSTORM imaging in a common optical platform to obtain new insights into the cytoskeleton's interplay with the plasma membrane, which supports the formation of fenestrations in LSECs. Ring-shaped total internal reflection fluorescence (TIRF) excitation on the same SIM platform was used to evenly excite and localize single molecules, albeit with a limited field of view (FOV).[31] Most recently, Tinguely et al. combined chip-based TIRF dSTORM with focused ion beam scanning electron microscopy (FIB-SEM) to demonstrate wide-field imaging, super-resolution nanoscopy and 3D electron microscopy for cell biology applications.[35] Although CLEM provides an attractive means to zoom into the complex organization of cells with highest resolution, it is challenged by the loss of fluorescence upon the use of chemical fixatives and heavy metals as well as dehydration artifacts resulting from EM sample preparation.[34,35] Therefore, all-optical correlative super resolution microscopy that enables the identification of cells/areas of interest in a fast acquisition mode and which could then be followed by a higher resolution modality to identify relevant features across a large FOV would be preferred. Here, we present the correlative SRM imaging of intracellular structures of LSECs across different microscope platforms (3D-SIM and dSTORM) facilitated by a transparent polymer photonic waveguide chip. This combination utilizes the advantages of each individual super- resolution modality while the chip-based TIRF excitation also provides a large FOV. In addition, the photonic chip is used as a sample holder to easily move samples between different setups. The use of transparent chips, with objective underneath, would be more amenable to observe living cells in culture media.

2. Results and Discussion

LSECs are a special type of endothelial cell with unique morphology and function. They contain a large number of nanopores in their plasma membrane, known as fenestrations, with a diameter of ≈ 50–300 nm. These transcellular "true" holes are usually clustered together in groups of 10–100, called liver "sieve plates". LSECs fenestrations funnel through the cell and provide an open pore system capable of size-dependent filtering waste molecules, nanoparticles, and viruses from the blood. Lipoproteins and pharmaceuticals taken up via the digestive system to the blood are also able to pass through the fenestrations.[38–41] The shape, diameter, and number of fenestrations can be altered in, for example, liver disease, aging, and drug interactions etc.[39,41] Hence, the detailed visualization of the ultrastructural morphology of LSECs is important in order to analyze a cells' structural viability and sieving function. In our correlative super-resolution imaging approach, first a rapid 3D-SIM image of LSECs is taken to confirm the presence of fenestrations within the cell. Then the exact size and morphology of LSECs fenestrations are verified by subsequent dSTORM measurements with higher spatial resolution on another instrument. To register the different instruments with sub-micron reproducibility, the waveguides themselves serve as guides, because they provide sufficient contrast under white light illumination and their photolithographically prepared edges are steeper than the resolution limit of a diffraction-limited microscope. Therefore, correlative SIM and waveguide TIRF based dSTORM imaging allows for the fast identification of LSECs even on separate instruments. Furthermore, waveguide based dSTORM provides high throughput imaging through its large FOV of ≈180 µm × 120 µm to resolve the intricate substructure of individual fenestrations with high spatial resolution (≈45 nm – limited by and scaling with the numerical aperture of the objective lens) and a significantly reduced background.

To evaluate the potential of correlative super-resolution microscopy the performance of 3D SIM (3D-SIM) and waveguide chip based TIRF dSTORM were demonstrated by imaging fenestrations in fixed rat LSECs seeded directly on the waveguide surface. Schematics describing the sample preparation on top of transparent polymer waveguide chips, image acquisition on a 3D-SIM setup, as well as the coupling of laser light and the detection optics of the custom-built photonic chip-based microscope, are shown in **Figure 1**. The excitation laser beam (EB) propagates through the waveguide core material and generates an evanescent field (EF) on top of the waveguide surface due to total internal reflection. A LSECs suspension is placed on top of the photonic chip resulting in cells attaching themselves either entirely on top of the waveguide surface, entirely on the cover

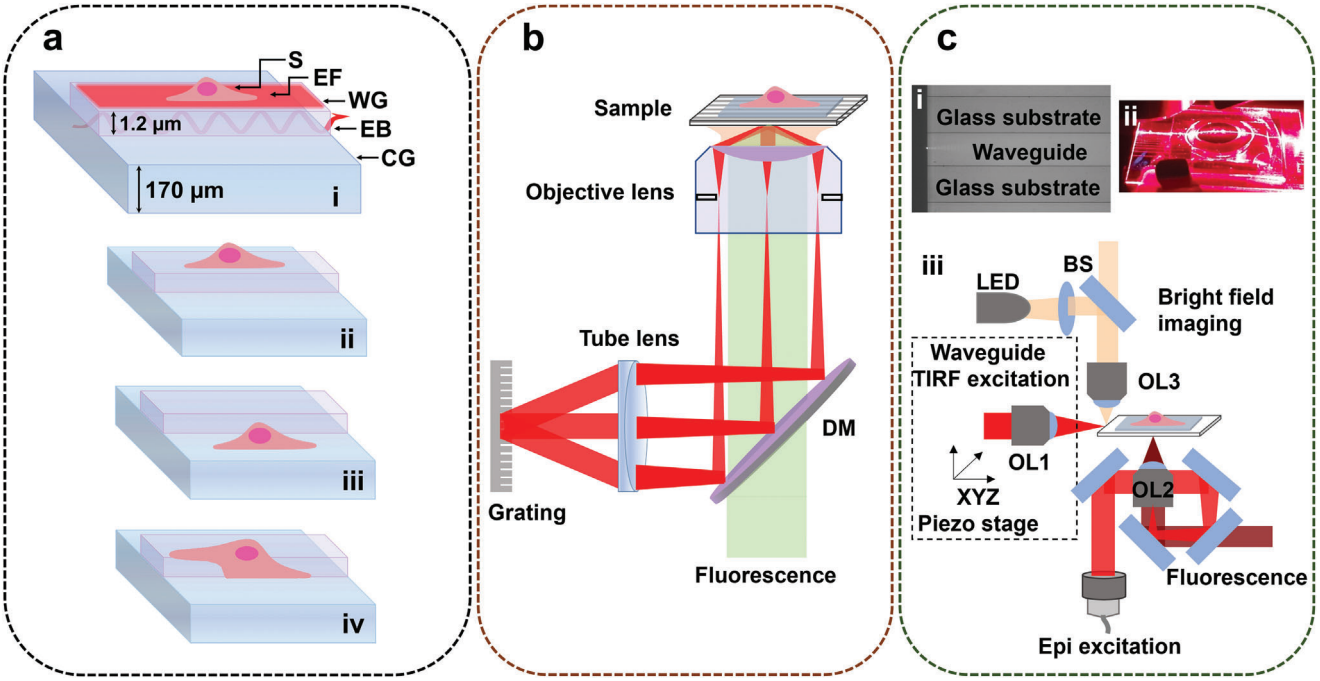

Figure 1. Schematic representation of the transparent polymer waveguide chip, 3D-SIM and waveguide chip- based nanoscopy setups. a) Waveguide geometry and working principle of chip-based TIRF microscopy. Transparent planar polymer waveguides (substrate: EpoCore with refractive index, n = 1.59 for λ = 647 nm) with a thickness of 1.2 µm were fabricated on top of a standard #1.5 borosilicate microscope coverslips (thickness: 170 µm). (i) Upon coupling light into the front facet, the excitation laser beam propagates through the waveguide core material due to total internal reflection and generates an evanescent field on top of the waveguide surface that excites fluorescent dyes in the sample. Liver sinusoidal endothelial cells (LSECs) are allowed to attach to different surfaces: (ii) cells that are attached entirely on top of the waveguide surface, (iii) cells that are attached entirely to the coverslip substrate, and (iv) cells that are attached partially to the waveguide surface and to the coverslip. b) Schematic overview of the 3D-SIM setup. A sinusoidal illumination pattern is created by the interference of three laser beams in the sample plane. Cells representing the different attachment scenarios (ii)–(iv) can all be illuminated with this striped excitation pattern. The fluorescence signal is detected by the same objective lens and transmitted through a dichroic mirror to the camera. c) Schematic representation of the waveguide chip-based dSTORM microscopy setup. (i) Bright field top view image of a waveguide on top of the glass substrate. The small bright white spot on the left-hand side shows the point where laser light is coupled into the input facet of the waveguide. Different waveguides are separated from each other by 200 µm of coverslip substrate to form a photonic chip. (ii) Photograph of the photonic chip held in an inverted optical microscopy setup. A red excitation laser beam is coupled into and highlights one of the waveguides. (iii) Schematic of the epi-illumination and waveguide TIRF based dSTORM setup. This setup consists of an objective lens (OL1) mounted on a xyz piezo stage to facilitate easy coupling of the excitation beam into the waveguide. Fluorescence emission of the sample is collected by a second objective lens (OL2) through the transparent substrate. This objective lens is also used for epi-illuminated fluorescence excitation. The bright field imaging unit of the setup consists of a white LED for illumination, a beam splitter, an objective lens (OL3) and a camera. It allows inspection of the input facet of waveguide during laser beam coupling. Abbreviations: S—sample, EF—evanescent field, WG—waveguide, EB—excitation beam, CG—cover glass, DM— dichroic mirror, BS—beam splitter, and OL—objective lens.

glass substrate, or partially to the waveguide surface and coverslip respectively (Figure 1a-ii–iv). The schematic overview of the 3D-SIM setup is shown in Figure 1b. A sinusoidal striped illumination pattern was created by the interference of three laser beams in the sample plane. Cells in all three potential conditions (attached on top of the transparent waveguide surface, on the coverslip, or partially on both surfaces) are illuminated with this excitation pattern. The fluorescence signals are collected by the objective lens and transmitted through a dichroic mirror and a long pass filter to the camera. Schematic representations of the custom-built waveguide chip-based super-resolution microscopy setup and the coupling of excitation light into the photonic chip are shown in Figure 1c. The sideways coupling and waveguide TIRF excitation generate an evanescent field on the top of the waveguide surface with a penetration depth of ≈150 nm that is used to excite all fluorescent markers located within this small zone above the waveguide surface. The details of the waveguide design and layout, different FOV measurements, and the illumination pattern uniformity are explained in supporting information Figure 1 (Figure S1, Supporting Information).

It is important to mention here that the polymer-based photonic waveguide chip enables the switching of epiexcitation and waveguide-based TIRF excitation because of the transparent nature of the substrates. Furthermore, it allows for the collection of fluorescence emission in a common inverted microscope configuration.

To investigate potential differences in cell adhesion and to evaluate the imaging quality of samples sitting on top of polymer waveguide surfaces we first carried out the 3D-SIM imaging of LSECs attached to the top of the cover glass and waveguide surfaces separately. **Figure** 2a,b shows 3D-SIM images of fixed rat LSECs attached on top of the cover glass and the polymer waveguide surface, respectively. The inset shows the enlarged view of

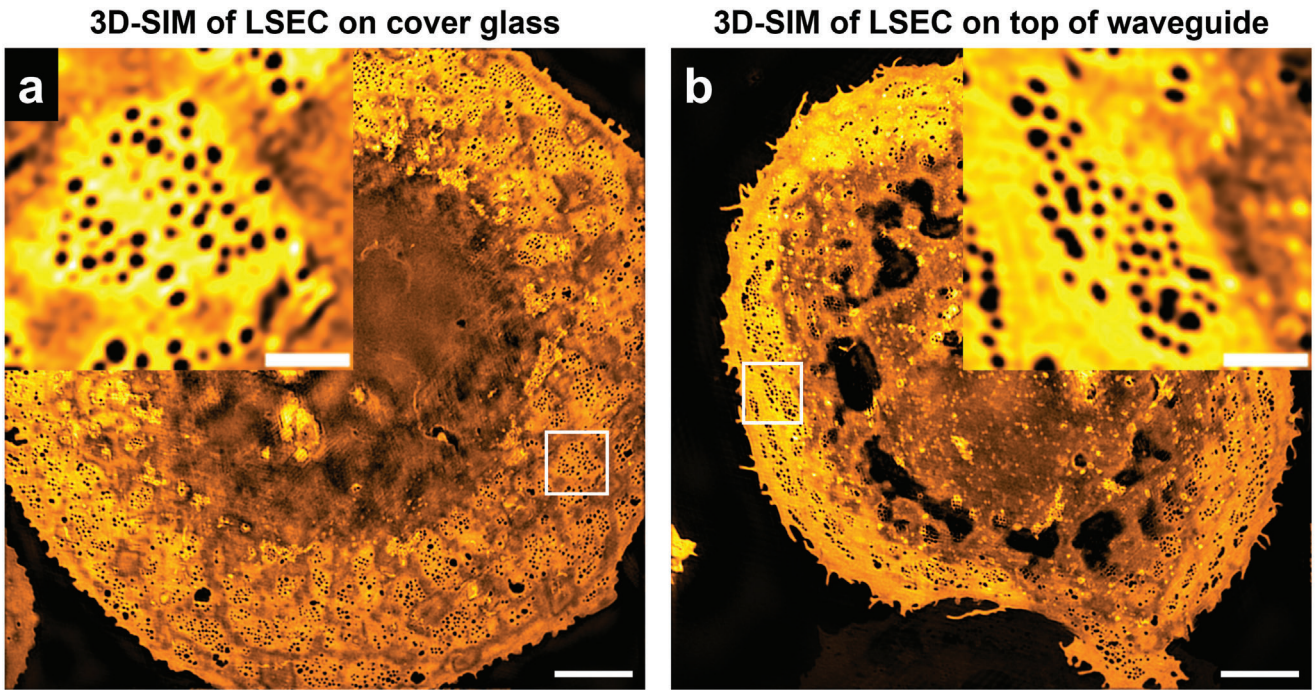

Figure 2. 3D-SIM images of fixed rat liver sinusoidal endothelial cells (LSECs) attached on top of the cover glass and the waveguide surface, respectively. a) 3D-SIM image of a representative LSEC attached to the cover glass substrate. Inset shows the enlarged view of the location marked with a white box. b) 3D-SIM image of a LSEC that is attached on top of the 1.2 µm thick polymer waveguide surface. Inset shows the enlarged view of the location marked with a white box. Both the SIM images show several sieve plates containing numerous fenestrations with diameters well below the diffraction limit. As can be seen from these representative examples, the SIM image reconstruction process is not notably affected by imaging through the additional polymer waveguide layer. The spatial resolution of both images is determined by image decorrelation analysis and are 171 nm (for a) and 174 nm (for b), respectively. The cell membrane is stained with BioTracker 655 dye. Scale bars: 5 µm; insets 1 µm.

the areas marked with white boxes. Both SIM images show several sieve plates containing numerous fenestrations. This result suggests that neither the SIM image acquisition nor the SIM image reconstruction process are affected by imaging through the additional polymer waveguide layer. We determined the spatial resolution of both images via image decorrelation analysis and obtained 171 nm (for Figure 2a) and 174 nm (for Figure 2b), for red excitation light ($\lambda = 642$ nm). The lack of any differences in LSEC morphology between the two substrates suggests no effect on cell attachment and well-being on the waveguide substrate.

Furthermore, to ensure that the transparent polymer waveguide surface truly does not interfere with the SIM image acquisition and reconstruction process, we also collected 3D-SIM images from a fixed rat LSEC where one part of the cell had attached to the waveguide surface and the other part of the cell to the cover glass substrate as shown in **Figure 3**. Figure 3a presents the reconstructed 3D-SIM image of the part of the cell that was sitting on top of the 1.2 µm thick transparent polymer waveguide surface. The reconstructed 3D-SIM image of the other part of the LSEC that is attached to the cover glass is shown in Figure 3b. To better visualize the reconstruction quality and fenestrations the enlarged view of the areas (Figure 3a,b) highlighted by white boxes are also presented in Figure 3d,e. Here, we find that the various sieve plates and fenestrations of LSEC are clearly visible in both parts of the cell. To visualize the boundary of the waveguide surface and glass substrate the maximum intensity projection of the 3D-SIM reconstruction of a 1.5 µm thick z-stack of the entire LSEC was performed and is presented in Figure 3c. The border between the waveguide and the glass surface is apparent by the dark line in the image. It is even more visible in the orthogonal view (right hand side), which also reveals the height difference of 1.2 µm between the different parts of the cells. Once it was confirmed that the transparent polymer waveguide surface does not interfere in the cell adhesion, imaging, and reconstruction, we continued to perform the photonic chip assisted correlative 3D-SIM and dSTORM imaging of LSECs to take advantage of the specific strengths of each technique.

To evaluate the ability of correlative super-resolution microscopy for better visualization and correlation of LSEC fenestrations we first measured 3D-SIM and epi-dSTORM images of rat LSECs seeded on top the fibronectin-coated photonic chips (**Figure 4**). Here, the waveguide structures served purely as guides to find the same cells on the different setups. The comparison of the diffraction-limited wide-field fluorescence, the corresponding 3D-SIM, and epi-dSTORM images of a LSEC attached on top of the cover glass substrate are shown in Figure 4a–c, respectively. The corresponding enlarged views of the areas marked by white boxes are also shown (Figure 4i–iii). As expected, significantly improved spatial resolution of the fenestrations by 3D-SIM and dSTORM compared to the wide field image is observed. Hence, in a similar manner the diffraction limited, 3D-SIM, and epi-dSTORM imaging of LSECs that were attached to the 1.2 µm thick waveguide surface was performed and the resulting images

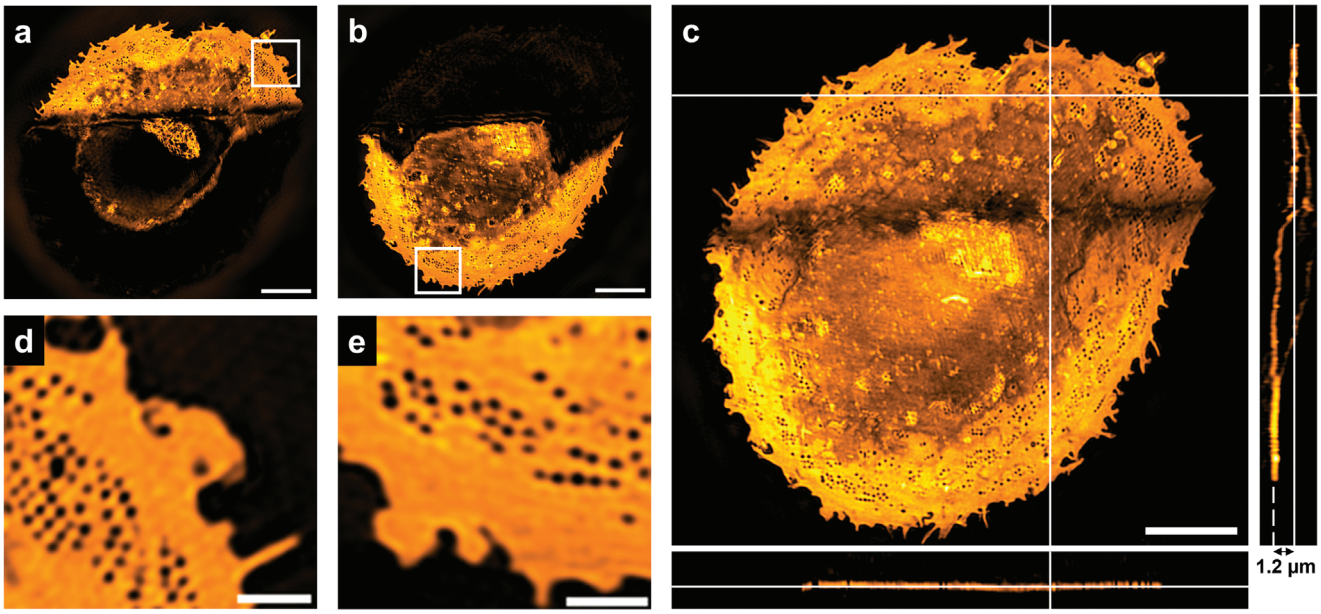

Figure 3. 3D-SIM image of a fixed rat LSEC partially attached to the waveguide surface and the cover glass surface. a) Reconstructed 3D-SIM image of the part of the cell that is sitting on top of the 1.2 µm high transparent polymer waveguide surface. b) Reconstructed 3D-SIM image of the lower part of the LSEC attached to the cover glass. d,e) Enlarged views of the regions of interest (white boxes) shown in (a,b). Sieve plates with fenestrations are clearly visible in both parts of the cell. c) Maximum intensity z-projection of the 3D-SIM image of the entire cell. The border between the waveguide and the glass surface is apparent by the dark line in the upper third of the image. It is even more visible in the orthogonal view (right hand side), which also reveals the height difference of 1.2 µm between the different parts of the cells. The cell membrane is stained with BioTracker 655 dye. Scale bars: a–c) 5 µm; insets d,e) 1 µm.

compared (Figure 4d–f—with corresponding magnified regions (Figure 4iv–vi)).

We were able to visualize and correlate the structural organization of LSEC fenestrations with gradually increasing spatial resolution in the order of 170 nm for 3D-SIM and 45 nm for epi dSTORM measurements. Spatial resolutions were calculated by image decorrelation analysis and Fourier ring correlation analysis for 3D-SIM and dSTORM measurements. It is important to mention here that in the enlarged views some fenestrations appear larger in size for the dSTORM measurement as compared to its 3D-SIM counterparts. Initially, we thought that this effect might be related to the dye used for staining the plasma membrane (BioTracker655). Overall, we found that the BioTracker dye gave us the best results based on its homogeneous and specific binding to the plasma membrane and it also allowed us to record a sufficient number of blinking events for dSTORM image reconstruction. Please note that in order to visualize fenestrations in the plasma membrane with a size of 50–300 nm in diameter, the membrane needs to be stained, hence resulting in a negative image of the fenestrations. We also found, however, that this dye, in combination with the dSTORM buffer, exhibits signal fluctuations even when it is not bound to the cell membrane. This behavior could have been an explanation for the appearance of a bigger fenestration size in the dSTORM images compared to their SIM counterparts. The limited resolution improvement of linear 3D-SIM and the convolution of the fluorescence signal with the microscope's optical transfer function, however, result in blurring of the stained parts of the sample – in this case the membrane. The membrane, thus, appears wider, resulting in an apparently reduced size of the hole. To visualize this phenomenon, we simulated holes with different diameters in a fluorescent environment and the resulting 2D images and reconstructed them (see Figure 4g). We found that the reconstructed SIM images always result in an apparently smaller diameter of the fenestrations than the actual size of the holes. In this case, 200 nm diameter holes are shown as having a width of ≈160 nm for red light excitation, as shown in the lower panel of Figure 4 (Figure 4g–i). Thus, although dSTORM also has its challenges for this type of sample, as detailed above, the correlation between these techniques is, indeed, very useful.

To take advantage of the transparent photonic chip's ability to excite the samples directly through the waveguide illumination, the waveguide TIRF/chip-based dSTORM measurement was illustrated by imaging of the fenestrations in LSECs. Here, waveguide TIRF-based microscopy results in evanescent field illumination of a thin bottom section of ≈150 nm thickness of the LSECs and the emitted fluorescence signal was collected through the transparent waveguide in the inverted mode (Figure 1c). This reduces the detection of additional signals due to scattering, refraction, and out of focus light during the imaging as compared to the upright configuration. **Figure** 5a,b shows the correlative 3D-SIM and waveguide TIRF dSTORM images of fenestrations within the same LSEC. The cell was seeded on top of the transparent polymer waveguide surface. Similarly, as before, enlarged overlays of the areas marked by white boxes are shown in the same figure (Figure 5c,d). Furthermore, to demonstrate the advantage of using dual modalities for imaging and the benefit of using transparent polymer waveguide chips for correlative super-resolution imaging we overlaid both, the 3D-SIM and waveguide TIRF dSTORM images of the same LSEC sitting on top

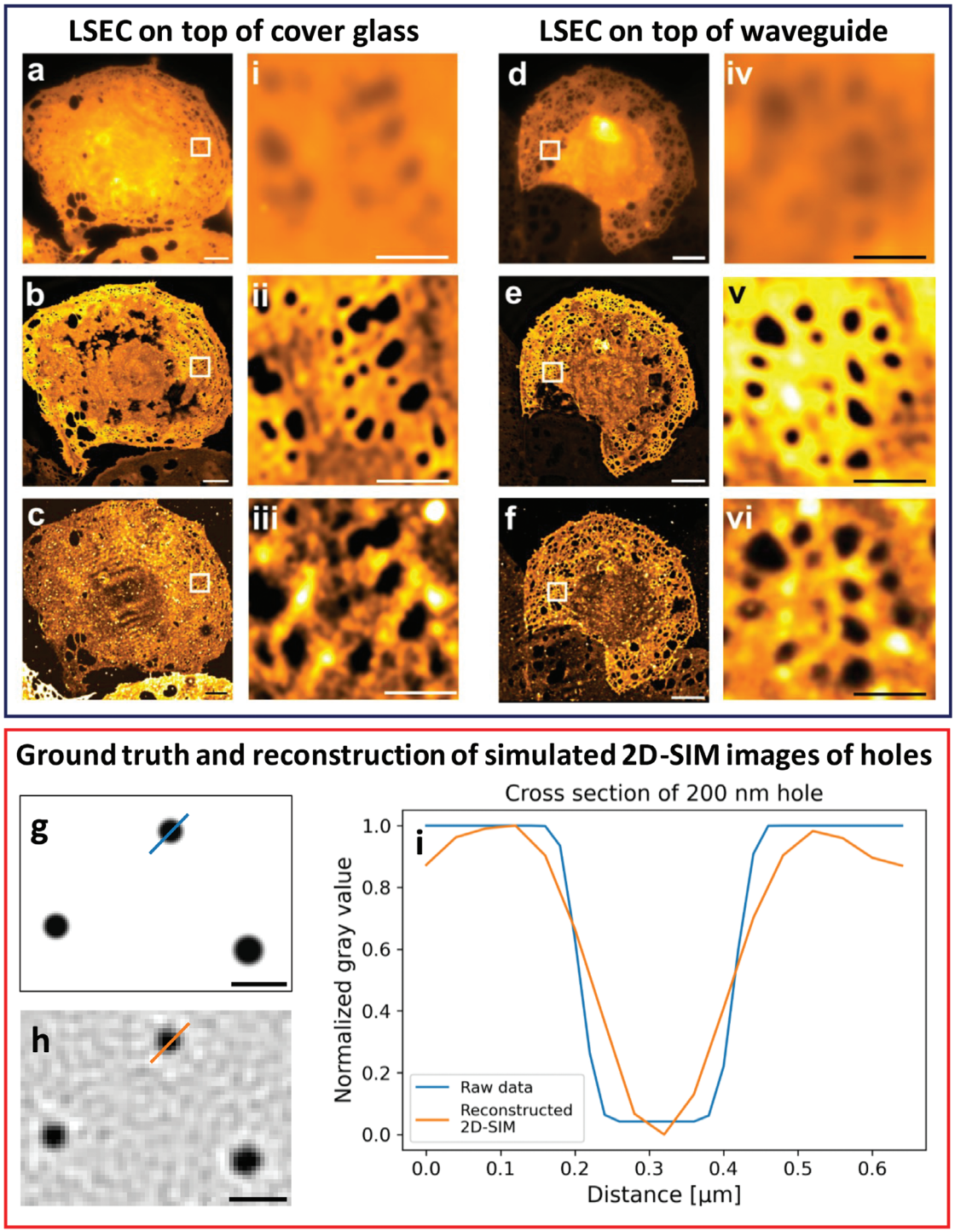

Figure 4. Correlative diffraction-limited wide field, 3D-SIM and epi-dSTORM images of fixed rat liver sinusoidal endothelial cells (LSECs). Blue box: The cell shown in the left two columns is attached to the cover glass substrate and the cell shown in the right two columns is attached to the 1.2 μm thick waveguide surface fabricated on top of the coverslip. a,d) Wide-field fluorescence images of the LSECs, where the optical diffraction limit prevents the fenestrations from being resolved. b,e) 3D-SIM reconstruction and c,f) corresponding epi-dSTORM images of the same LSECs. The fenestrations are well resolved in both the 3D-SIM and dSTORM images. (i–vi) Enlarged views of the corresponding regions of interest (ROIs) shown in (a–f). The cell membrane is stained with BioTracker 655 dye. The lower half, surrounded by a red box, shows the reconstruction of simulated 2D-SIM images of holes with different diameters within a fluorescent environment (g–i). The simulated hole with a diameter of g) 200 nm results in a reconstructed 2D-SIM image with a width of h) ≈160 nm. The comparison of the cross sections of the ground truth and the reconstructed image of a simulated hole is shown in (i). We found that the reconstructed SIM images always result in an apparently smaller diameter of the fenestrations than the actual size of the holes. Scale bars: a–f) 5 μm; insets 1 μm (i–vi); g,h) 500 nm.

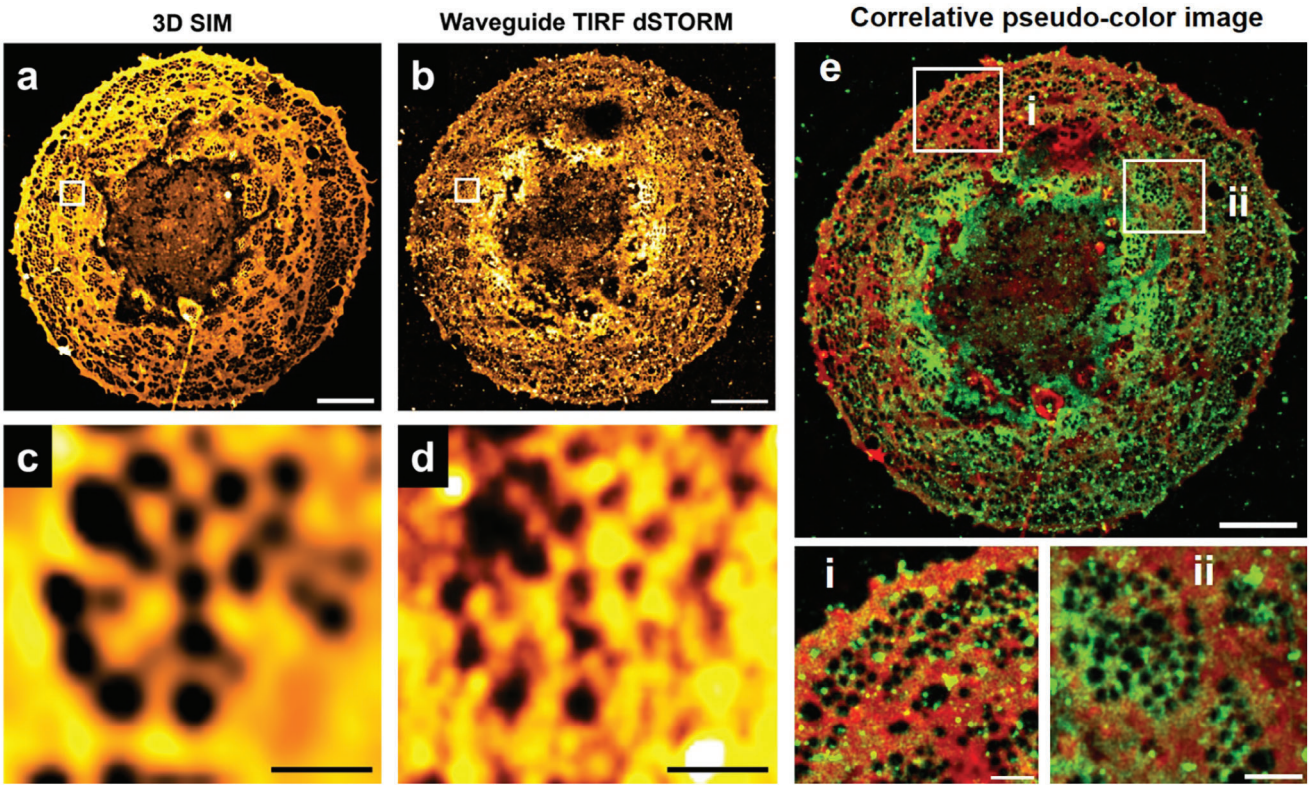

Figure 5. Correlative 3D-SIM and waveguide TIRF dSTORM images of a rat liver sinusoidal endothelial cell (LSEC). a) Reconstructed 3D-SIM image of LSEC placed on a 1.2 µm thick transparent polymer waveguide surface fabricated on top of a 170 µm thick borosilicate microscope coverslip substrate and c) enlarged view of the ROI (white box) shown in (a). b) Waveguide TIRF dSTORM reconstruction of same LSEC and d) enlarged view of corresponding ROI (white box) shown in (b). e) Correlative pseudo-color image of LSEC, where both, the 3D-SIM and waveguide TIRF dSTORM images of a LSEC sitting on top of the waveguide surface are overlaid. The same fenestrations are distinguished clearly in both the 3D-SIM and waveguide TIRF dSTORM reconstructions. The fenestrations in the SIM reconstruction appear with a round shape due to ≈170 nm spatial resolution provided by 3D-SIM. Their actual size and shape are identified in the corresponding waveguide TIRF dSTORM image with a spatial resolution of ≈50 nm. The cell membrane was stained with BioTracker 655 dye. Scale bars: a, b, e) 5 µm; insets 1 µm (c, d, and i, ii).

of the waveguide surface. This is demonstrated via a correlative pseudo-color image (Figure 5e). The overlaid image allows us to identify the LSEC fenestrations and correlate them for both imaging modalities with high spatial resolution. In order to find and properly overlay the correct cells imaged with both techniques, we relied on the waveguide structure as fiducial marker.

Correlative imaging shows that the same fenestrations are distinguished clearly in both the 3D-SIM and waveguide TIRF dSTORM reconstructed images. The fenestrations in the 3D-SIM reconstruction appear in round shape due to the limited 2X resolution gain. The higher resolved waveguide TIRF dSTORM images, however, reveal that the size and shape of the fenestrations differ and that individual fenestrations are not necessarily round by nature, but contain straight edges that are a result of the plasma membrane being wrapped around the actin cytoskeleton of the LSEC.[31,42] The overall resolution enhancement in the dSTORM images was determined by Fourier ring correlation (FRC) analysis and measured to be 49 nm as compared to 172 nm for 3D-SIM imaging (as measured by image decorrelation analysis).

In addition, the transparent waveguide chip also provides evanescent field excitation over a large FOV allowing simultaneous imaging of several cells as demonstrated in **Figure 6**. This configuration allows the use of objective lenses with different magnifications and numerical apertures to collect the fluorescence signal, enabling scalable FOV imaging.[23] By collecting the fluorescence through the transparent chip, the collection efficiency and spatial resolution can then be improved even further. The diffraction limited images of three different LSECs seeded on top a 120 µm wide waveguide surface as well as the corresponding waveguide TIRF excited dSTORM images are shown in Figure 6a,b. The FOV of 180 µm x 120 µm was obtained by collecting the fluorescence through the waveguide chip by using a 60×, 1.35 NA oil immersion objective lens. It is important to mention that some striped variations of the fluorescence intensity are visible on the cells in Figure 6a. This is attributed to the presence of multiple different modes propagating inside the waveguide, as well as interference effects between these modes, which results in a spatially stable distribution of laterally non-uniform evanescent fields. The resulting patterns depend strongly on how the laser light was coupled into the waveguide. Accordingly, the fluorescence excitation is inhomogeneous, which can also impair the reconstructed dSTORM images. To counteract this, a piezo stage was used to rapidly oscillate the objective lens that is used for coupling light into the waveguide back and forth along the input facet of the waveguide during the measurement. This maintains

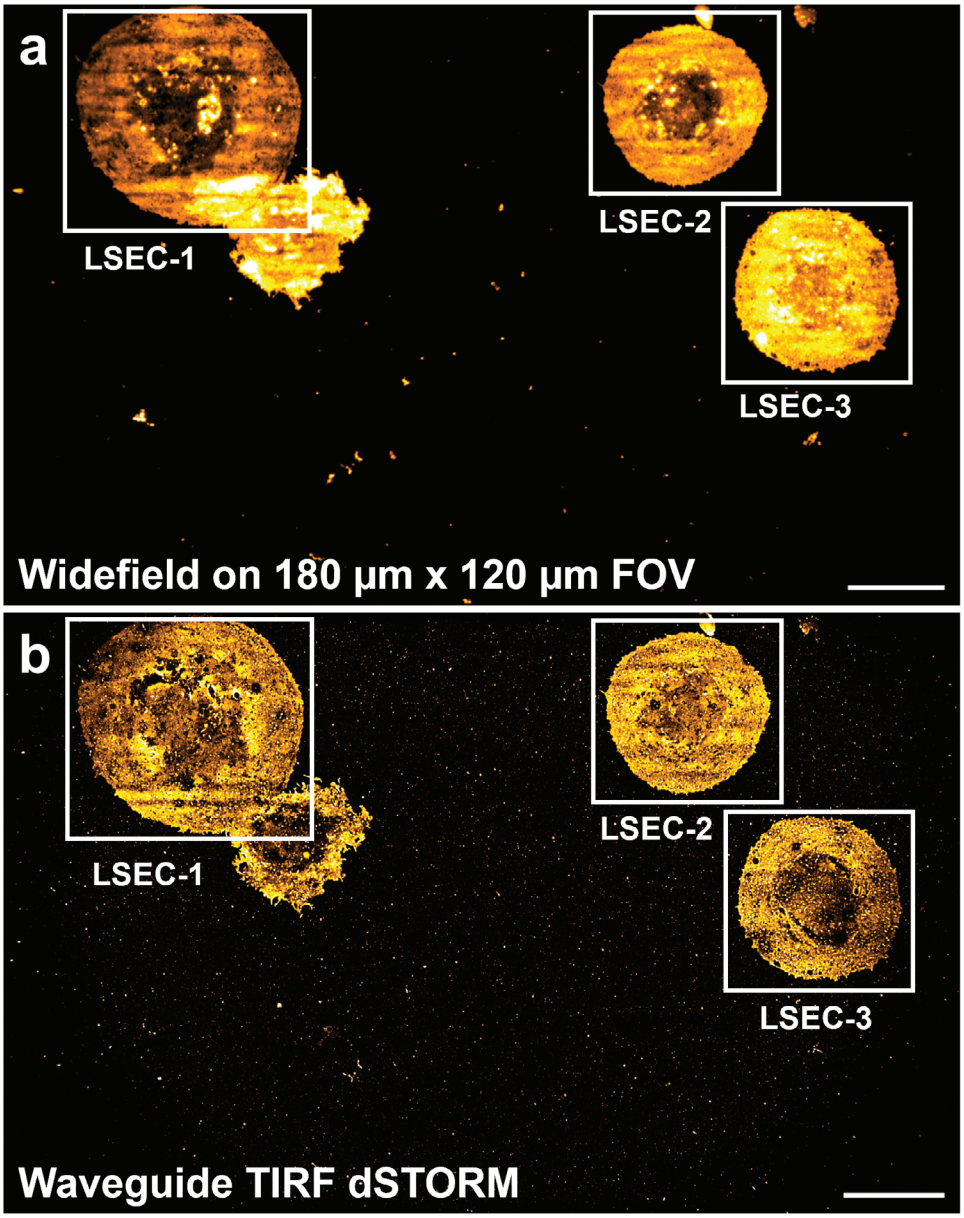

Figure 6. Large FOV widefield and waveguide TIRF dSTORM images (180 µm × 120 µm). The stripe pattern visible on the cells is due to the interference of multiple modes propagating through the waveguide, which varies depending on the spot where the laser light is coupled into the waveguide. For dSTORM image acquisition the beam of the excitation laser is swept along the input facet of waveguide to reduce the stripe artifacts. a) Diffraction limited fluorescence image of three different LSECs on top of a 120 µm wide polymer waveguide. b) Waveguide TIRF dSTORM image of the corresponding LSECs over the same FOV. The dSTORM reconstruction of 50000 frames results in a super-resolved image over the entire FOV. The spatial resolution as determined by Fourier ring correlation is ≈50 nm. The membrane of the LSECs is stained with BioTracker 655 dye. Scale bar: 20 µm.

efficient light coupling into the waveguide but continuously changes the mode pattern during dSTORM image acquisition. This results in the temporal averaging of fluorescence excitation by different modes and reduces the appearance of these patterns in the reconstructed dSTORM image (cf. Figure 6b). The dSTORM image reconstruction of 50000 individual frames then results in a super-resolved image across the entire FOV resulting in a spatial resolution of 48 nm as determined by FRC analysis.

By again exploiting the waveguides as visual markers, the waveguide TIRF-based dSTORM images can be correlated with 3D-SIM images obtained on a separate instrument as demonstrated in **Figure 7**. Figure 7a–c shows the 3D-SIM reconstructed images of individual LSECs obtained on the commercial DeltaVision|OMX v4. The FOV of this microscope is limited to approximately 40 µm x 40 µm. Therefore, three individual measurements and separate 3D-SIM reconstructions had to be performed to obtain these images of three different LSECs. The waveguide TIRF-based dSTORM image, on the other hand, provides the super-resolved full FOV in a single dSTORM measurement and images of the same cells that were measured individually by 3D-SIM can

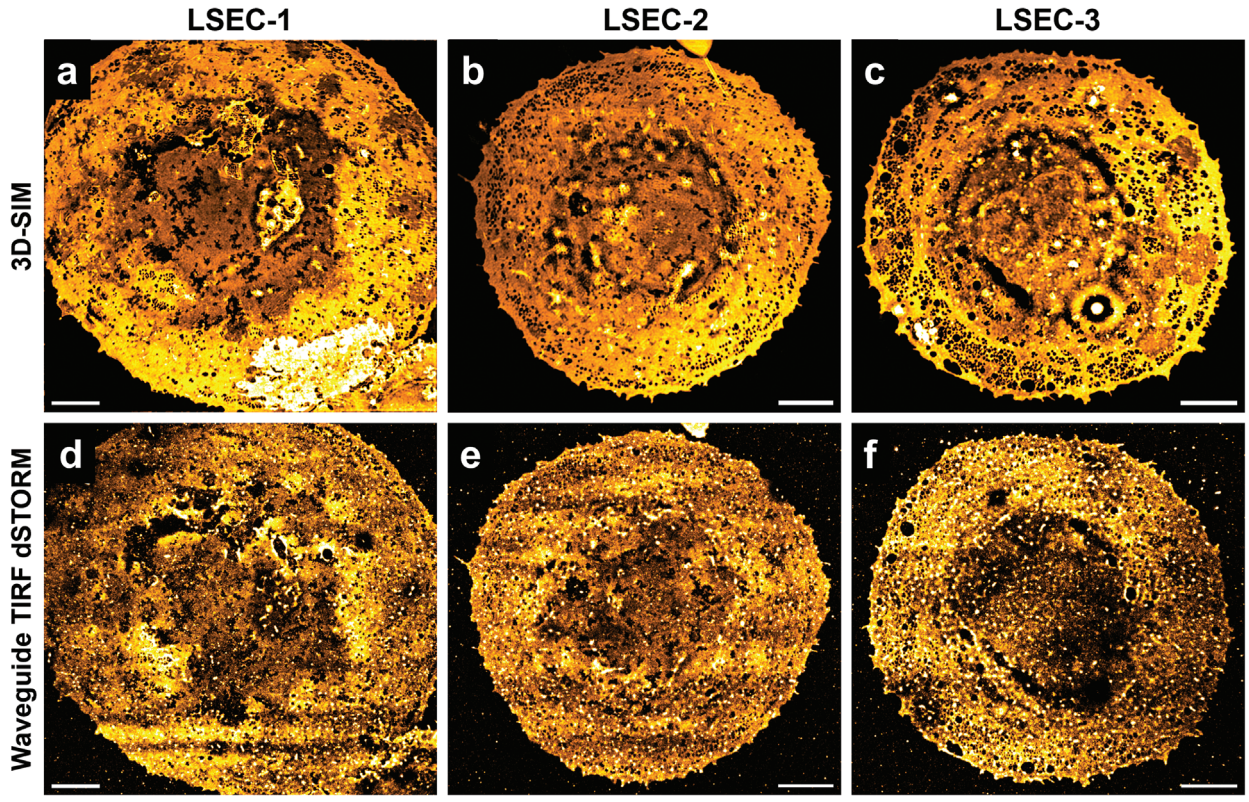

Figure 7. Correlative 3D-SIM and waveguide TIRF dSTORM images of three LSECs shown within the large FOV of 180 µm × 120 µm in Figure 6. a–c) Top row: 3D-SIM reconstructions of the cells. d–f) Bottom row: corresponding waveguide TIRF dSTORM reconstructions of the same cells. The FOV of the 3D-SIM reconstruction of the commercial OMX V4 is limited to approximately 40 µm × 40 µm. Therefore, three individual measurements were required to image three different cells, whereas the waveguide TIRF dSTORM provides the large FOV in a single dSTORM measurement. Scale bar: 5 µm.

now be compared to regions of interest from Figure 6b as shown in Figure 7d–f.

Please note that in addition to the different spatial resolution of the images collected with the different modalities, the waveguide TIRF-based dSTORM images were collected by exciting a just ≈150 nm thick part of the cells right above the waveguide surface, whereas the 3D-SIM images represent projected intensity images of a much larger volume of the cells. Furthermore, during the 3D-SIM measurement the specimen is excited with a fairly low laser power to minimize photo-bleaching of the sample. In waveguide TIRF mode, however, the entire specimen sitting on top of the waveguide is excited. In order to conduct dSTORM measurements and obtain a sufficient number of blinking events from single molecules, we have to increase the laser power to the maximum value that can be coupled into the end facet of the polymer waveguide (≈20 mW) without harming the waveguide. Therefore, the other parts of the sample that are not in the FOV of the microscope but on the same waveguide surface are photobleached during this measurement. The TIRF condition, however, limits photobleaching to the lowest ≈150 nm just above the waveguide surface.

3. Conclusion

Photonic waveguide chips have recently emerged as novel platforms for optical nanoscopy enabling the fluorescence imaging of samples across large fields of view with high spatial resolution in multiple modalities. The photonic chip serves two purposes: it provides a substrate to conveniently hold the sample, and it channels the laser light necessary for efficient fluorescence excitation with low background contributions. Here, we have demonstrated that a transparent polymer waveguide chip provides significantly improved chip-based TIRF imaging compared to traditional TIRF techniques. The polymer waveguide structures can be conveniently produced without the need for a specialized clean-room and the expensive equipment required for producing waveguide structures made from inorganic materials. We demonstrated that imaging with high numerical aperture lenses through the additional thin polymer waveguide has essentially no negative impact on the resulting fluorescence images. Indeed, the inverted microscopy configuration results in images with fewer aberrations and better resolution as compared to imaging structures on opaque waveguide chips in the upright configuration. The transparent chips also improved the LSEC samples preparation allowing for the assessment of cell seeding and quality before staining and imaging with super-resolution techniques. Therefore, the use of transparent chips, with objective underneath, would be more amenable to observing living cells in culture media. We further demonstrated that the polymer waveguide chips support the workflow for correlative light microscopy on different imaging platforms. We evaluated the performance of these photonic chips by comparing 3D-SIM and chip

based TIRF single molecule imaging techniques for the analysis of LSECs fenestrations. Although fenestrations can be imaged, identified and their numbers can be quantified by 3D-SIM, the resolution improvement of this method is limited to a factor of two, i.e., it ranges between 120 and 170 nm depending on the wavelength. This results in the representation of individual fenestrations as round objects, whereas higher resolving methods, such as dSTORM more accurately reveal that fenestrations are defined by actin fiber mesh, around which the plasma membrane appears to wrap. Photonic waveguide chips thus provide an excellent platform for complementary super-resolution imaging. While 3D-SIM is a rather fast super-resolution imaging method, its field of view is limited, and its spatial resolution is restricted. Waveguide-based dSTORM imaging, on the other hand, provides a large field of view with higher spatial resolution, although being time-consuming due to its need for having to collect thousands of images of blinking fluorescent molecules.

4. Experimental Section

Waveguide Chip Fabrication: The transparent waveguides were fabricated on top of a standard # 1.5 borosilicate microscope coverslip (thickness: 170 µm) as shown in Figure 1a. The photoresist polymer EpoCore (refractive index $n = 1.59$ for $\lambda = 647$ nm) was used as the core waveguide material and spin cast on top of the glass substrate. The detailed procedure of the photonic chip fabrication process was reported previously.[29,30] The mean height of the fabricated waveguides is ≈1200 ± 4 nm, and surface roughness, Sa = 5.5 ± 3.7 nm. The fabricated waveguide chips were cleaned using 0.1% sodium dodecyl sulfate (SDS) in water solution in a sonicator bath for 5 minutes. Subsequently, the chips were rinsed three times with 70% ethanol followed by distilled water. The surface was dried in a stream of pressurized nitrogen gas. Then, a transparent polydimethyl siloxane (PDMS) chamber with a volume of ≈200 µL was added on top of the waveguide chip to place the cell suspension inside it. Finally, the waveguide chips were stored in sterilized Petri dishes for further use.

Sample Preparation: Cryopreserved rat LSECs (adult male Sprague Dawley) were isolated following a previously published protocol[43] and stored at -80 °C in vials containing 1 mL cell suspension with ≈3×10^6 cells. The vials were placed in an incubator at 37 °C to thaw the cells. The waveguide chips were coated with human fibronectin (0.2 mg mL^{-1} in phosphate-buffered saline (PBS)) for 45 min at room temperature and washed twice with PBS. The thawed cells were gently pipetted into 24 mL pre-warmed RPMI 1640 media (11875093, ThermoFisher) and centrifuged at 50 g for 3 min to remove remaining hepatocytes (primary LSEC isolations have variable levels of hepatocyte contamination). The supernatant was used for a second centrifugation step at 300 *g* for 8 min to remove any remaining DMSO present in the freezing solution. The cell pellet was not clearly visible after the centrifugation. The supernatant was removed and 10 mL fresh RPMI media was added to the remaining solution and centrifuged again at 300 *g* for 8 min. Then 200 µL of cell pellet was added to the PDMS chamber on top of the waveguide chip surface and incubated at 37 °C with 5% CO_2. The media was changed after 1 h of incubation and the cells spent another 2 h in the incubator before the experiment. The cells were then fixed with 4% paraformaldehyde (PFA) in PBS solution for 10 min at room temperature and were washed three times with PBS. Afterward, the LSEC membrane was stained with 1:200 BioTracker 655 dye (SCT108, Merck) in PBS for 45 min at room temperature and finally the cells were washed three times with PBS solution.

Correlative Imaging: In the first step of measurements, 3D-SIM images of LSECs were acquired using a commercial SIM microscope (Deltavision OMXv4.0 BLAZE, GE Healthcare). The system is an inverted microscope, which means that the illumination light must penetrate through the glass coverslip (thickness: 170 µm) and the additional 1.2 µm thick polymer waveguide to excite the cells attached to the waveguide surface (Figure 1b). A red laser diode with $\lambda = 642$ nm was used to excite the membrane-stained cells. For 3D-SIM measurements, the excitation laser power was set such that on the one hand sufficient fluorescence signal from the cells was obtained for artifact-free 3D reconstruction and on the other hand to minimize photobleaching of the sample. In this case, the SIM excitation laser power was ≈7 mW at the back focal plane of the objective lens. 1.5 µm high z-stacks with a step size of 0.125 µm and 15 raw images per slice (3 angles with 5 phases each) were captured for each cell. The raw images were reconstructed using the SoftWorX package from GE Healthcare to obtain the final 3D-SIM images. The reconstruction results with SoftWorX are, in essence, the same as those obtained with other open-source SIM reconstruction tools such as Open-3D-SIM,[44] because both use the same underlying Gustafsson algorithm for reconstructing SIM data.[7]

The field of view (FOV) of the SIM reconstruction is limited to 40.96 µm x 40.96 µm which means that only one cell could be imaged in one frame. Before SIM measurement, a stable and nonfluctuating buffer system, which contains reducing as well as oxidizing agents (ROXS) without thiols, was added to minimize photobleaching of the sample during measurement.[45] This allowed further use of the same sample for correlative dSTORM measurements. After the SIM measurements, the ROXS buffer solution was removed, and PBS was added to the cells. Hence, the layout of the waveguide chip was used to identify the exact position of each cell for correlative dSTORM measurements. A single photonic chip consists of several waveguides with different widths varying from 10 to 200 µm, and the waveguides are separated from each other by a distance of 200 µm of coverslip substrate.[29,30]

A custom-built setup was used for the waveguide TIRF-based dSTORM measurement. The details of the setup and the procedure for coupling laser light into the waveguide chips were also reported previously.[29,30] In brief, an Ar-Kr+ ion laser (Innova 70C Spectrum, Coherent) was used as the laser source. The laser line at 647 nm wavelength with ≈150 mW laser power was selected using an acousto-optic tunable filter. The output laser beam was directed to the coupling optics on top of a Thorlabs NanoMax 300 xyz-piezo stage (MAX312D, Thorlabs Inc). A long working distance 20×, 0.35 NA objective lens (SLMPlan, Olympus) was used to focus the beam onto the input facet of the polymer waveguide. Focus spot optimizations for WG TIRF illumination and minimization of interference streak patterns were done by controlling the xyz piezo stage position. A 60X, 1.35 NA oil immersion objective lens (UPlanSApo, Olympus) was used to collect the fluorescence emission as well as for epi excitation. The single-molecule localization microscopy (SMLM) raw image stacks were acquired with an uncooled industry-grade CMOS camera (UI-3060CP-MGL, IDS Imaging Development Systems) with a 1936×1216-pixel sensor and a pixel size of 5.86 µm x 5.86 µm. The upright microscope was used to investigate the waveguide input facets during the measurement as shown in Figure 1c. The transparent nature of the polymer waveguide chip allows to switch between the WG-based TIRF illumination and epi illumination on a single microscopy setup.

It is crucial to select the appropriate buffer solution for SMLM measurements. The common GODCAT buffer system[22] was used containing enzymatic oxygen scavengers, glucose oxidase, and catalase with mercaptoethylamine (MEA) as a switching agent. The stock solutions of enzymes, glucose, and MEA were prepared according to van de Linde et al.[22] and stored at −20 °C until the use for dSTORM measurements. Furthermore, to verify that there is no change of TIRF excitation conditions due to a change of the index of refraction of the buffer solutions, the indices of refraction (RI) of all solutions including doubly ionized (DI) water using a BAUSCH & LOMB table top refractometer (Serial No. 032115R) were measured and compared. It is found that there is no significant change in the RI and it stays below $n = 1.352$ for all of the buffer solutions that was used during the sample preparation and measurements. This is, in essence, similar to the RI of water, i.e., approximately $n = 1.33$, which is significantly lower than the refractive index of the polymer waveguide ($n = 1.59$ at approximately 650 nm). This ensures that the TIRF excitation condition is always met. A table of the RI of all solutions used in this paper is presented in Table S1 (Supporting Information).

For epi-dSTORM experiments, a total of 30000 frames were acquired with a camera exposure time of 50 ms at ≈ 0.4 kW cm^{-2} laser power using the 647 nm laser line. For localization microscopy facilitated by excitation through the polymer waveguide chips (WG TIRF dSTORM) the maximum laser power at the front facet of the waveguides was ≈ 20 mW. That allowed to induce sufficient fluorophore blinking for dSTORM image reconstruction without destroying or burning the soft polymer waveguide material. The acquisition time was 50 ms per frame and a total of 50 000 frames were recorded and used for image reconstruction. The super-resolution dSTORM images were reconstructed by the open-source comprehensive super-resolution microscopy analysis platform (SMAP) from the series of acquired raw images.[46] Finally, the localization tables are imported in ImageJ via the Plugin ThunderSTORM,[47] and visualized as average shifted histograms. Furthermore, to get a better comparison of the excitation laser power in both setups, the fluorescence emissions of 100 nm size TetraSpeck microspheres using both 3D-SIM and waveguide TIRF dSTORM imaging techniques were measured. The excitation laser power for both methods was adjusted to achieve the same fluorescence intensity of the microspheres. The fluorescence emission of 100 nm beads shows nearly the same gray values for ≈15 mW excitation power for 3D-SIM and 22 mW at the end facet of the waveguide for TIRF dSTORM measurements, respectively, although there is no direct correlation of the incident laser power between the setups. Figure S2 (Supporting Information) illustrates this statement.

Supporting Information

Supporting Information is available from the Wiley Online Library or from the author.

Acknowledgements

This study was supported by the European Union's European Innovation Council (EIC) PATHFINDER Open Programme under grant agreement No. 101046928. Part of the project also received funding from the Deutsche Forschungsgemeinschaft (DFG), grant number 540217954 to T.H. The authors thank Prof. Dr. Andreas Brockhinke for the use of their instrument for refractive index measurements.

Open access funding enabled and organized by Projekt DEAL.

Conflict of Interest

The authors declare no conflict of interest.

Data Availability Statement

The data that support the findings of this study are available from the corresponding author upon reasonable request.

Keywords

correlative microscopy, polymer waveguides, single-molecule localization microscopy, structured illumination microscopy, super-resolution optical microscopy

Received: October 14, 2024
Revised: November 25, 2024
Published online:

[1] C. Eggeling, K. I. Willig, S. J. Sahl, S. W. Hell, *Q. Rev. Biophys.* **2015**, *48*, 178.
[2] S. J. Sahl, S. W. Hell, S. Jakobs, *Nat. Rev. Mol. Cell Biol.* **2017**, *18*, 685.
[3] S. W. Hell, *Science* **2007**, *316*, 1153.
[4] E. Betzig, G. H. Patterson, R. Sougrat, O. W. Lindwasser, S. Olenych, J. S. Bonifacino, M. W. Davidson, J. Lippincott-Schwartz, H. F. Hess, *Science* **2006**, *313*, 1642.
[5] L. Schermelleh, R. Heintzmann, H. Leonhardt, *J. Cell Biol.* **2010**, *190*, 165.
[6] M. G. L. Gustafsson, *J. Microsc.* **2000**, *198*, 82.
[7] M. G. L. Gustafsson, L. Shao, P. M. Carlton, C. J. R. Wang, I. N. Golubovskaya, W. Z. Cande, D. A. Agard, J. W. Sedat, *Biophys. J.* **2008**, *94*, 4957.
[8] S. W. Hell, J. Wichmann, *Opt. Lett.* **1994**, *19*, 780.
[9] K. I. Willig, S. O. Rizzoli, V. Westphal, R. Jahn, S. W. Hell, *Nature* **2006**, *440*, 935.
[10] M. Lelek, M. T. Gyparaki, G. Beliu, F. Schueder, J. Griffié, S. Manley, R. Jungmann, M. Sauer, M. Lakadamyali, C. Zimmer, *Nat. Rev. Methods Primers* **2021**, *1*, 39.
[11] M. J. Rust, M. Bates, X. Zhuang, *Nat. Methods* **2006**, *3*, 793.
[12] M. Tokunaga, N. Imamoto, K. Sakata-Sogawa, *Nat. Methods* **2008**, *5*, 159.
[13] T. Dertinger, R. Colyer, G. Iyer, S. Weiss, J. Enderlein, *Proc. Natl. Acad. Sci. USA* **2009**, *106*, 22287.
[14] I. Yahiatene, S. Hennig, M. Müller, T. Huser, *ACS Photonics* **2015**, *2*, 1049.
[15] R. F. Laine, H. S. Heil, S. Coelho, J. Nixon-Abell, A. Jimenez, T. Wiesner, D. Martínez, T. Galgani, L. Régnier, A. Stubb, G. Follain, S. Webster, J. Goyette, A. Dauphin, A. Salles, S. Culley, G. Jacquemet, B. Hajj, C. Leterrier, R. Henriques, *Nat. Methods* **2023**, *20*, 1949.
[16] C. G. Galbraith, J. A. Galbraith, *J. Cell Sci.* **2011**, *124*, 1607.
[17] J. Valli, A. Garcia-Burgos, L. M. Rooney, B. Vale de Melo e Oliveira, R. R. Duncan, C. Rickman, *J. Biol. Chem.* **2021**, *297*, 100791.
[18] H. Ortkrass, J. Schürstedt, G. Wiebusch, K. Szafranska, P. McCourt, T. Huser, *Opt. Express* **2023**, *31*, 29156.
[19] H. Ortkrass, G. Wiebusch, J. Linnenbrügger, J. Schürstedt, K. Szafranska, P. McCourt, T. Huser, *Opt. Express* **2023**, *31*, 40210.
[20] A. Sandmeyer, M. Lachetta, H. Sandmeyer, W. Hübner, T. Huser, M. Müller, *ACS Photonics* **2021**, *8*, 1639.
[21] A. Markwirth, M. Lachetta, V. Mönkemöller, R. Heintzmann, W. Hübner, T. Huser, M. Müller, *Nat. Commun.* **2019**, *10*, 4315.
[22] S. van de Linde, A. Löschberger, T. Klein, M. Heidbreder, S. Wolter, M. Heilemann, M. Sauer, *Nat. Protoc.* **2011**, *6*, 991.
[23] R. Diekmann, Ø. I. Helle, C. I. Øie, P. McCourt, T. R. Huser, M. Schüttpelz, B. S. Ahluwalia, *Nat. Photonics* **2017**, *11*, 322.
[24] L. E. Villegas-Hernández, V. Dubey, M. Nystad, J.-C. Tinguely, D. A. Coucheron, F. T. Dullo, A. Priyadarshi, S. Acuña, A. Ahmad, J. M. Mateos, G. Barmettler, U. Ziegler, Å. B. Birgisdottir, A.-M. K. Hovd, K. A. Fenton, G. Acharya, K. Agarwal, B. S. Ahluwalia, *Light: Sci. Appl.* **2022**, *11*, 43.
[25] A. Archetti, E. Glushkov, C. Sieben, A. Stroganov, A. Radenovic, S. Manley, *Nat. Commun.* **2019**, *10*, 1267.
[26] Ø. I. Helle, D. A. Coucheron, J.-C. Tinguely, C. I. Øie, B. S. Ahluwalia, *Opt. Express* **2019**, *27*, 6700.
[27] N. Jayakumar, F. T. Dullo, V. Dubey, A. Ahmad, F. Ströhl, J. Cauzzo, E. M. Guerreiro, O. Snir, N. Skalko-Basnet, K. Agarwal, B. S. Ahluwalia, *Nanophotonics* **2022**, *11*, 3421.
[28] A. Priyadarshi, F. T. Dullo, D. L. Wolfson, A. Ahmad, N. Jayakumar, V. Dubey, J.-C. Tinguely, B. S. Ahluwalia, G. S. Murugan, *Commun. Mater.* **2021**, *2*, 85.
[29] A. K. Engdahl, S. Belle, T.-C. Wang, R. Hellmann, T. Huser, M. Schüttpelz, *ACS Photonics* **2021**, *8*, 1944.
[30] A. K. Engdahl, S. B. Dutta, S. Belle, J. Schürstedt, K. Szafranska, P. McCourt, R. Hellmann, T. Huser, M. Schüttpelz, *bioRxiv* **2022**, 2022.11.29.518375.
[31] V. Mönkemöller, C. Øie, W. Hübner, T. Huser, P. McCourt, *Sci. Rep.* **2015**, *5*, 16279.

[32] S. Rossberger, G. Best, D. Baddeley, R. Heintzmann, U. Birk, S. Dithmar, C. Cremer, *J. Opt.* **2013**, *15*, 094003.
[33] V. Hamel, P. Guichard, M. Fournier, R. Guiet, I. Flückiger, A. Seitz, P. Gönczy, *Biomed. Opt. Express* **2014**, *5*, 3326.
[34] K. Szafranska, T. Neuman, Z. Baster, Z. Rajfur, O. Szelest, C. Holte, A. Kubisiak, E. Kus, D. L. Wolfson, S. Chlopicki, B. S. Ahluwalia, M. Lekka, M. Szymonski, P. McCourt, B. Zapotoczny, *Nanophotonics* **2022**, *11*, 2253.
[35] J.-C. Tinguely, A. M. Steyer, C. I. Øie, Ø. I. Helle, F. T. Dullo, R. Olsen, P. McCourt, Y. Schwab, B. S. Ahluwalia, *Commun. Biol.* **2020**, *3*, 739.
[36] C. van Rijnsoever, V. Oorschot, J. Klumperman, *Nat. Methods* **2008**, *5*, 973.
[37] W. Kukulski, M. Schorb, S. Welsch, A. Picco, M. Kaksonen, J. A. G. Briggs, *J. Cell Biol.* **2011**, *192*, 111.
[38] K. K. Sørensen, J. Simon-Santamaria, R. S. McCuskey, B. Smedsrød, *Compr. Physiol.* **2015**, *5*, 1751.
[39] K. Szafranska, L. D. Kruse, C. F. Holte, P. McCourt, B. Zapotoczny, *Front. Physiol.* **2021**, *12*, 735573.
[40] K. K. Sørensen, P. McCourt, T. Berg, C. Crossley, D. L. Couteur, K. Wake, B. Smedsrød, *Am. J. Physiol.: Regul., Integr. Comp. Physiol.* **2012**, *303*, R1217.
[41] C. I. Øie, V. Mönkemöller, W. Hübner, M. Schüttpelz, H. Mao, B. S. Ahluwalia, T. R. Huser, P. McCourt, *Nanophotonics* **2018**, *7*, 575.
[42] B. Zapotoczny, K. Szafranska, M. Lekka, B. S. Ahluwalia, P. McCourt, *Int. J. Mol. Sci.* **2022**, *23*, 9850.
[43] V. Mönkemöller, H. Mao, W. Hübner, G. Dumitriu, P. Heimann, G. Levy, T. Huser, B. Kaltschmidt, C. Kaltschmidt, C. I. Øie, *Sci. Rep.* **2018**, *8*, 14657.
[44] R. Cao, Y. Li, X. Chen, X. Ge, M. Li, M. Guan, Y. Hou, Y. Fu, X. Xu, C. Leterrier, S. Jiang, B. Gao, P. Xi, *Nat. Methods* **2023**, *20*, 1183.
[45] J. Vogelsang, R. Kasper, C. Steinhauer, B. Person, M. Heilemann, M. Sauer, P. Tinnefeld, *Angew. Chem., Int. Ed.* **2008**, *47*, 5465.
[46] J. Ries, *Nat. Methods* **2020**, *17*, 870.
[47] M. Ovesný, P. Křížek, J. Borkovec, Z. Švindrych, G. M. Hagen, *Bioinformatics* **2014**, *30*, 2389.